Strain engineering of magnetic and orbital order in perovskite $LuMnO_3$ epitaxial films

Chao Ji,[1] Yancheng Wang,[1] Bixiang Guo,[1] Xiaofan Shen,[1] Qunyong Luo,[1] Jianli Wang,[1] Xianwen Meng,[1] Junting Zhang,[1,*] Xiaomei Lu,[2] and Jinsong Zhu[2]

[1]*School of Physical Science and Technology, China University of Mining and Technology, Xuzhou 221116, China*

[2]*National Laboratory of Solid State Microstructures and Physics School, Nanjing University, Nanjing 210093, China*

(Received 15 July 2019; revised manuscript received 20 September 2019; published 12 November 2019)

Epitaxial strain has been extensively used to tailor the functionality of perovskite oxides, in which strain control of magnetism is highly desirable, especially for perovskite manganites. Here on the basis of the first-principles calculations we demonstrated the control of magnetic phase and orbital order in $LuMnO_3$ film by epitaxial strain imposed by a square substrate and revealed the surface and interface effects by combining the strain-bulk and heterostructure models. The spiral and E-type multiferroic phases present in perovskite manganites bulks can exist in the tensile strained films, while a ferromagnetic half-metal phase with high Curie temperature and an antiferromagnetic polar-metal phase arise in the range of compressive strain. Increasing compressive strain changes the sign of the Q_3 mode of Jahn-Teller distortion, resulting in the transition of the in-plane stagger orbital order to a uniform orbital order. The reconstruction of Jahn-Teller distortion and orbital order occur in the first two layers near the surface. The symmetry breaking of the crystal field at the surface leads to a uniform $d_{3z^2-r^2}$ type orbital order and surface metallization. The electron accumulation at the interface with $SrTiO_3$ substrate has been demonstrated and decreases dramatically with the increase in the number of $LuMnO_3$ layers.

DOI: 10.1103/PhysRevB.100.174417

I. INTRODUCTION

Perovskite oxides exhibit a wide range of functional properties due to the coupling between lattice, charge, orbital, and spin degrees of freedom [1–3]. Small external perturbations, such as epitaxial pressure, tend to change their functionality owing to the close energy between the various interactions [4–6]. With the development of film deposition technology, epitaxial strain has become an important means to tune the functionality of material, providing an additional degree of freedom in materials design [7–10]. For example, the epitaxial strain can stabilize the ferroelectric phase of $SrTiO_3$ [11] and induce ferroelectric ferromagnetic (FM) phase in paraelectric antiferromagnets by means of spin-lattice coupling [12,13].

Perovskite manganites $RMnO_3$ (R = La-Lu), which exhibit fascinating properties such as colossal magnetoresistance [1], phase separation [14], and magnetically driven multiferroics [15], have recently shown more abundant strain effects [16–21]. The epitaxial strain imposed by $SrTiO_3$ substrate can drive the magnetic phase transition from antiferromagnetic (AFM) to FM in some $RMnO_3$ [16,19,22], while the (010)-oriented $YAlO_3$ substrate stabilizes the E-type multiferroic phase for the whole series of $RMnO_3$ [21,23]. In addition, the coexistence of multiple magnetic phases has also been observed experimentally [17,24], which may be attributed to the existing strain gradient in strained films [22,25]. Therefore, it is promising to achieve the desired functionality in $RMnO_3$ films by controlling the magnetic phase via strain engineering, for which a wide variety of perovskite substrates provide a great opportunity [26,27].

Previous studies on strain effects of $RMnO_3$ films have focused on a fixed substrate to reveal the evolution of the magnetic phase with rare-earth R ions. However, it has been shown that the $RMnO_3$ films may be subjected to different strain levels due to stress relaxation, which depends on film thickness and growth conditions [28]. Our recent studies have shown that a single strained $RMnO_3$ film, especially for R ions near the end of the $RMnO_3$ series, can exhibit complex magnetic phase diagram with the change in strain levels [22]. Therefore, it is crucial to understand the detailed evolution of magnetic phases with strain levels in order to accurately control the magnetic phase. In addition, the surface and interface effects, which may play an important role in very thin $RMnO_3$ films, were ignored in previous studies based on the bulk models.

In this paper, by combining the strained-bulk and heterostructure models, we studied the surface and interface effects and the variation trend of structural, magnetic, electronic, and ferroelectric properties with epitaxial strain imposed by the square substrates. We focus on the $LuMnO_3$ film, which is at the end of the $RMnO_3$ series. We demonstrated that the tensile strain causes the appearance of the spiral and E-type multiferroic phases, while the compressive strain leads to a half-metal FM phase and a AFM polar-metal phase. The in-plane staggered orbital order can be transformed into a uniform orbital order by a large compressive strain. We confirmed the reconstruction of orbital order and the metallization near the surface. The electron accumulation at the interface decreases dramatically with the increase in the number of $LuMnO_3$ layers.

*juntingzhang@cumt.edu.cn

II. COMPUTATIONAL DETAILS

The density-functional-theory (DFT) calculations were performed using the projector-augmented wave method [29] with generalized gradient approximation (GGA) of the Perdew-Burke-Ernzerhof functional, as implemented in the Vienna *ab initio* simulation package (VASP) [30]. Our previous studies have confirmed that the GGA method can well reproduce the magnetic phase diagrams of $R\mathrm{MnO_3}$ bulks and strained films, and the introduction of the on-site Coulomb repulsion parameter (GGA + U) method would overestimate the tendency of exchange interactions toward ferromagnetism, resulting in the predicted magnetic phase being inconsistent with the experimental results [23]. We demonstrated this again by checking the accuracy of the GGA + U method in predicting the magnetic phase of $\mathrm{LuMnO_3}$ bulk. We tested different U values in the range of 1–5 eV with a fixed exchange parameter $J = 1$ eV. The results show that only a very small U value ($U_{\mathrm{eff}} = U - J < 1$ eV) can reproduce the E-type magnetic ground state of $\mathrm{LuMnO_3}$ bulk (Fig. S1 [31]).

The GGA functional usually underestimates the band gap, especially for strongly correlated electronic systems. It has been shown that the hybrid exchange-correlation functional allows us to improve the consistency of the band gap with experiment for perovskite oxides [32–34]. Taking $\mathrm{LuMnO_3}$ bulk as an example, we compared the difference of projected band structures calculated by PBE and hybrid functional HSE methods. The inclusion of Hartree-Fock exchange in the HSE functional significantly increases the Jahn-Teller (JT) splitting between the occupied and unoccupied e_g orbitals, resulting in a band gap of 2.5 eV, much larger than the value of 0.4 eV calculated by PBE functional (Fig. S2 [31]). Meanwhile, the magnetic moment of Mn ion increases slightly, accompanied by a decrease in p-d hybridization compared with PBE functional. However, the band dispersion and orbital projection calculated by the HSE functional are similar to those of the PBE functional. In this study, the PBE functional is still used, since HSE calculation is very time consuming and there is currently no experimental value of band gap for $\mathrm{LuMnO_3}$ bulk to compare the accuracy of the two functionals.

For the strain-bulk models, the in-plane lattice parameters are fixed to be the same as the substrate to maintain epitaxial matching, while the out-of-plane lattice parameter and atomic positions are optimized until the residual force is less than 0.01 eV/Å to obtain the equilibrium structure. Due to the difference of the in-plane lattice parameters of $\mathrm{LuMnO_3}$ bulk, it is subjected to anisotropic strain imposed by the square substrates. For simplicity, the epitaxial strain is defined as $\varepsilon = (d - d_0)/d_0$, where d is the in-plane lattice constant of the square substrate and $d_0 = 5.484$ Å represents the geometric mean of two in-plane lattice constants of $\mathrm{LuMnO_3}$ bulk. It has been shown that the $R\mathrm{MnO_3}$ films can grow and maintain orthorhombic structure on the substrate with larger lattice mismatch [27]. For example, the lattice mismatches of $\mathrm{TmMnO_3}$ film grown on Nb-doped $\mathrm{SrTiO_3}(110)$ substrate are -4.94% and 6.72% along the b and c axes, respectively, and the $\mathrm{YbMnO_3}$ film on $\mathrm{SrTiO_3}(100)$ substrate suffer a tensile strain of 5.83% along the a axis and a compressive strain of -4.59% along the b axis [35]. Although the critical strain on a square substrate is unknown, a wide range of strain was used to clearly reveal the change trend of structural distortions and magnetic properties with epitaxial strain.

Similar to previous procedure, the collinear magnetic orders such as FM, and A-, C-, G-, E_b-, E_b^*-, E_a-, E_a^*-type, and the noncollinear spiral and spiral* spin orders were considered in the calculations of magnetic ground state. The symbols with an asterisk denote the same in-plane spin configuration as the corresponding symbol without an asterisk but with a FM interplanar coupling. E_a- and E_b-type orders represent the $\uparrow\uparrow\downarrow\downarrow$ spin chain arranged along the a and b axes, respectively, wherein the latter is the E-type phase present in $R\mathrm{MnO_3}$ (R = Ho-Lu) bulks. The spiral and spiral* spin orders are simulated using the $a \times 3b \times c$ orthorhombic supercell, corresponding to a wave vector number $q = 1/3$ close to that of $R\mathrm{MnO_3}$ bulks. The $5 \times 5 \times 3$, $5 \times 3 \times 3$, and $5 \times 2 \times 3$ Γ-centered k-point samplings were used for the calculations of unit cell, double and triple supercells, respectively. According to our tests, the calculation errors in relative energy of different magnetic orders due to the use of different k-point samples were less than 1 meV per unit cell. A plane-wave cutoff energy of 500 eV was used in the calculations with a convergence threshold of 10^{-6} eV. The spin-orbit coupling is included in the calculations of magnetic anisotropy energy, while it is switched off in the calculations of magnetic ground state, since it has only a slight influence on the relative energy of different magnetic orders.

For the heterostructure models, we chose the most commonly used $\mathrm{SrTiO_3}$ substrate, which imposes a tensile strain of $\sim 0.7\%$ on the $\mathrm{LuMnO_3}$ film. At the interface of heterostructures, the $\mathrm{TiO_2}$ termination was adopted according to the experimental results [19], and the bottom SrO layer was fixed during the structural relaxation to mimic a thick substrate. Previous theoretical study has shown that two perovskite layers with the fixed bottom layer are sufficient to simulate the effect of the $\mathrm{SrTiO_3}$ substrate [36]. In addition, our test results confirm that increasing the number of $\mathrm{SrTiO_3}$ layers slightly adjusts the relative energy of the magnetic orders without changing the magnetic ground state (Fig. S3 [31]). Therefore, the heterostructure models $(\mathrm{LuMnO_3})_n/(\mathrm{SrTiO_3})_2$ with different numbers of $\mathrm{LuMnO_3}$ layers was used, where n (=2,4,6) denotes the number of perovskite layer. A vacuum space of more than 15 Å was used in the supercell to separate the neighbor images along the vertical direction due to the periodic condition. The dipole moment correction was used to balance the difference in electrostatic potential on the two sides of the heterostructure due to the use of an asymmetric slab. For the calculations of unit cell and supercells of the heterostructures, the $5 \times 5 \times 1$ and $5 \times 2 \times 1$ k-point samplings were employed, respectively. Previous DFT calculations have shown that the GGA + U method ($U_{\mathrm{eff}} = 4.34$ eV for the $3d$ states of Ti ion) more accurately describes the structural and electronic properties of $\mathrm{SrTiO_3}$ [37], so we employed this method in the calculations of heterostructures, in which a small value of $U_{\mathrm{eff}} = 0.5$ eV was adopted for Mn ion according to the test mentioned above.

On the basis of the Heisenberg model and DFT-derived magnetic exchange parameters, the magnetic transition temperature was estimated by using the classical Monto Carlo (MC) simulations. We employed a $12 \times 12 \times 12$ cubic grid with periodic boundary conditions, and 10^6 MC steps with the

Metropolis algorithm were performed for each temperature. The energy density and the specific heat were calculated as functions of temperature, and the peak of specific heat was identified as the magnetic transition temperature. Our test results show that the MC simulations using the magnetic exchange parameters derived from GGA and GGA + U ($U_{\text{eff}} = 0.5$ eV) calculations overestimate and underestimate the transition temperature of $LuMnO_3$ bulk, respectively. Therefore, the calculated transition temperature based on the GGA calculations can be considered as the upper limit of the actual transition temperature of $LuMnO_3$ films.

III. RESULTS AND DISCUSSION

A. Structural distortions

We first investigated the effect of epitaxial strain on structural distortions. The orthorhombic structure of $LuMnO_3$ is caused by two types of structural distortion: The JT distortion and the rotation distortion of oxygen octahedron, whose strength can be evaluated from the differences in the lengths of three Mn-O bonds in oxygen octahedron and the deviation of Mn-O-Mn bond angles from 180°, respectively. For the two types of Mn-O bonds approximately lying in the *ab* plane, the longest Mn-O_1 bond (referring to the unstrained state) is significantly elongated with the increase of epitaxial strain, while the shortest Mn-O_2 bond remains basically unchanged, as shown in Fig. 1(a). This indicates that the Mn-O_2 bond is quite rigid, which has been reflected in previous studies on strained $RMnO_3$ films [22,23]. The length of the interplane Mn-O_3 bond monotonously decreases as the strain increases, consistent with the change trend of the *c*-axis lattice constant. Interestingly, when the compressive strain exceeds a certain value, the interplane Mn-O_3 bond replaces the Mn-O_1 bond as the longest bond, suggesting a transition of JT distortion.

The JT distortion can be specified by decomposing the structural distortion into the normal Q_2 and Q_3 modes, which represent the orthorhombic and tetragonal distortions of oxygen octahedra, respectively [38], as shown in Fig. 1(b). Their strength is defined as $Q_2 = (m - s)/\sqrt{2}$, $Q_3 = (2l - m - s)/\sqrt{6}$, where l, m, and s denote the length of the longest, middle, and shortest Mn-O bonds, respectively. The Q_3 mode is dominant in $RMnO_3$ bulks and causes a staggered orbital order in the *ab* plane. It is significantly weakened with the decrease of strain, consistent with the change of Mn-O_1 bond length, and becomes negative when the compressive strain exceeds the critical value by about −3%. This transition of Q_3 mode is rare for $RMnO_3$ and leads to the change of the in-plane orbital order [inset of Fig. 1(a)]. Contrary to the trend of the Q_3 mode, the Q_2 mode is gradually reduced to a small negative value as the strain increases, indicating the suppression of the Q_2 mode by tensile strain.

The out-of-plane Mn-O-Mn bond angle monotonically decreases with the increase of strain, due to the direct coupling between the tilt distortion of oxygen octahedra and the *c*-axis lattice constant, as shown in Fig. 1(c). The in-plane bond angle exhibits an approximate parabolic trend with its maximum at zero strain. This means that both compressive strain and tensile strain increases the in-plane rotation distortion of oxygen octahedra under the constraint of square substrates.

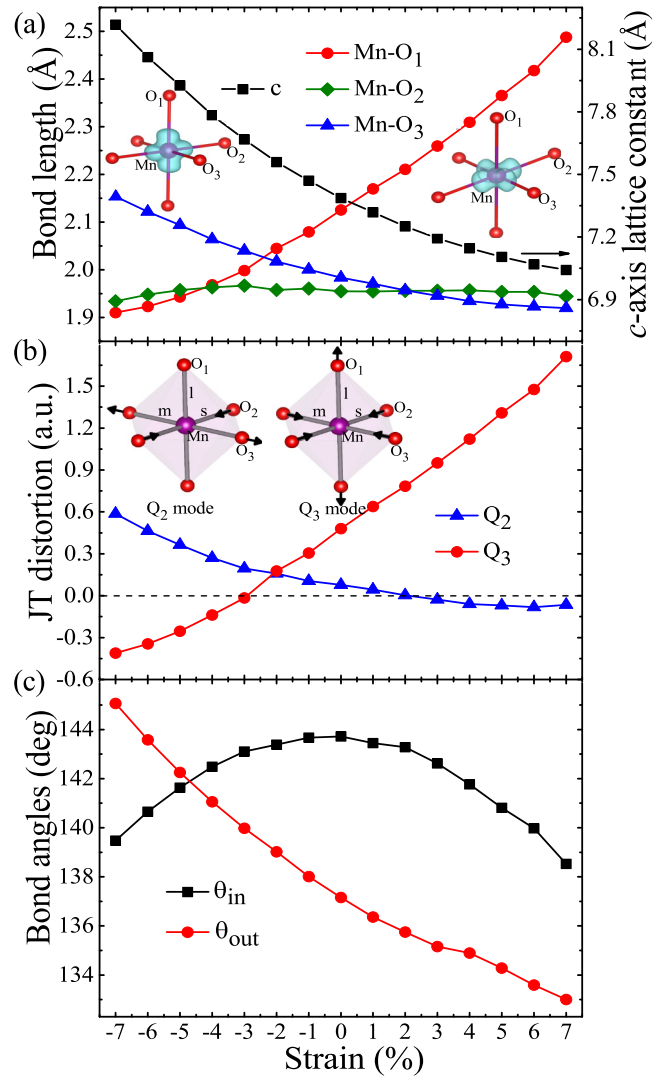

FIG. 1. Change of (a) three Mn-O bond length and *c*-axis lattice constant, (b) Q_2 and Q_3 modes of JT distortion, and (c) the in-plane (θ_{in}) and out-of-plane (θ_{out}) Mn-O-Mn bond angles with strain. The insets in (a) show the shape of the unoccupied *d* orbital (i.e., *d* hole) under large tensile and compressive strain. The insets in (b) show the structural distortion corresponding to the normal Q_2 and Q_3 modes.

This trend may be attributed to a faster increase in Mn-O_1 bond length with respect to the in-plane lattice constant and suggests a strong coupling between JT distortion and the in-plane rotation distortion of oxygen octahedra.

B. Magnetic properties

The total energy of all considered magnetic orders was calculated using the optimized structure under various strain in order to determine the evolution of the magnetic phase with strain. It should be noted that the actual size of the wave vector of spiral spin order in strained films is likely to deviate greatly from the case $q = 1/3$ used in the DFT calculation, so the DFT-calculated values cannot accurately represent the lowest energy of spiral spin order. Since the actual wave vector is dependent on the magnetic exchange interactions,

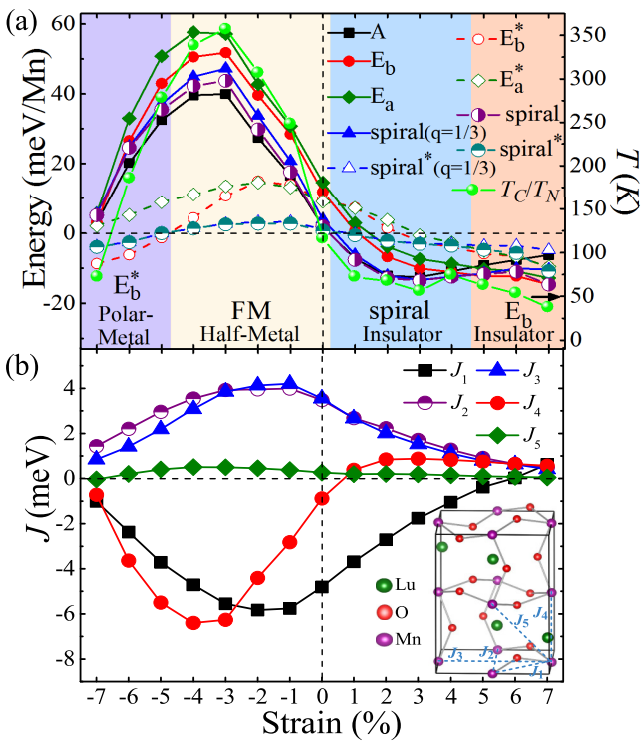

FIG. 2. (a) Relative energy (to FM order) of all AFM orders and magnetic transition temperature estimated by MC simulations as a function of strain. The relative energy of spiral and spiral* orders was calculated by the proposed energy minimization method. The relative energy of the higher-energy *C*- and *G*-type orders is not shown for clarity. (b) Magnetic exchange interactions calculated according to the Heisenberg model.

we calculated the lowest energy of spiral order by means of the energy minimization method based on the extracted magnetic exchange interactions. According to the Heisenberg model $H = \sum_{ij} J_{ij}\mathbf{S}_i \cdot \mathbf{S}_j$, where J_{ij} represents the considered nearest-neighbor (NN) and next-nearest-neighbor (NNN) magnetic exchange parameters, and $\mathbf{S}_i$ is the spin of Mn^{3+} ion, the dependence of the total energy of spiral order per unit cell on the wave vector number q can be written by

$$E(q) = (8J_1 \cos \pi q + 4J_2 \cos 2\pi q + 4J_3 - 4J_4 - 16J_5 \cos \pi q)S^2 + E_0. \quad (1)$$

$S = 2$ denotes the spin quantum number, and E_0 denotes the nonmagnetic energy term. J_1 and J_4 represent the NN exchange interactions along the in-plane and interplane directions, respectively [inset of Fig. 2(b)]. J_2 and J_3 represent the in-plane NNN exchange interactions along the b and a axes, respectively, and J_5 represents the interplane NNN exchange interaction. The lowest energy of spiral order can be obtained by solving the condition of energy minimization $\frac{\partial E}{\partial q} = 0$. This method yields a slight energy benefit (maximum of 17 meV within the strain range) for the spiral order with respect to the DFT-calculated value with $q = 1/3$.

The energy of all AFM orders (relative to FM order) as a function of epitaxial strain is shown in Fig. 2(a). At zero strain, for which a and b axes are subjected to tensile and compressive strain relative to the bulk, respectively, the magnetic ground state changes to a FM half-metal phase. It exists in a fairly wide range of compressive strain. Previous theoretical studies have predicted that this FM half-metal phase exists in some $R\mathrm{MnO_3}$ under compressive strain [39,40]. In addition, the strain-induced FM phase has been observed experimentally in some $R\mathrm{MnO_3}$ films grown on square substrates [16,19,41,42], such as $\mathrm{TbMnO_3}$ film grown on $\mathrm{SrTiO_3}(100)$ substrate [16,41], which is in the range of compressive strain. The MC simulations show that its Curie temperature can reach above room temperature within a specific strain range. This strain-induced high Curie temperature in manganites has been observed in $\mathrm{LaCaMnO_3}$ films grown on $\mathrm{SrTiO_3}(100)$ substrate [20]. As the compressive strain is further enhanced, the E_b^*-type order, which has the same in-plane spin configuration as the E-type phase but has a parallel interplane arrangement, turns into the magnetic ground state, accompanied by a rapid decrease in the magnetic transition temperature. Previous theoretical study has predicted that the energy of this E_b^*-type metal phase becomes nearly degenerate with the FM ground state in $\mathrm{EuMnO_3}$ under high pressure [40]. This magnetic phase was predicted for the first time to exist in strained $R\mathrm{MnO_3}$ films. Importantly, our previous studies have suggested that strain gradient present in $R\mathrm{MnO_3}$ films may lead to the coexistence of ferroelectric (E or E^* type) and FM phases, and a magnetoelectric coupling interface may be formed at the phase boundary between the E^*-type and FM phases [22]. However, the spin-induced electric polarization in this E_b^*-type phase should be screened due to its metal behavior.

In the region of tensile strain, the energy difference between magnetic orders is reduced overall, resulting in a significant reduction in the magnetic transition temperature compared with compressive strain. An insulated spiral phase replaces the FM phase as the magnetic ground state when a very small tensile strain is imposed. However, it should be noted that this magnetic ground state is subject to the competition of A-type order, indicated by their very close energy in the region of spiral phase [see Fig. 2(a)]. This result is similar to the case of the $\mathrm{YMnO_3}$ film grown on $\mathrm{SrTiO_3}$ substrate, in which a spiral or A-type magnetic phase, or even a mixed phase between them, may occur depending on the film thickness [43]. As the tensile strain increases further, the magnetic ground state is transformed into the E-type phase. Its maximum transition temperature reaches ~63 K, which is greater than the value of $\mathrm{LuMnO_3}$ bulk (36 K) and the highest value (41 K) present in $R\mathrm{MnO_3}$ films with the E-type phase [21]. These results indicate that the spiral and E-type multiferroic phases present in $R\mathrm{MnO_3}$ bulks can exist in the tensile strained $\mathrm{LuMnO_3}$ films, and the strain may improve their magnetic transition temperature with respect to the bulk phases.

Then we investigated the change of magnetic exchange interactions with epitaxial strain to explain the evolution of magnetic phases. Previous studies have confirmed that ignoring the higher-order spin interactions in the spin model only has little influence on the calculated values of magnetic exchange interactions [22,23], so the calculated energy of all magnetic orders was mapped to the above Heisenberg model (see Supplemental Material [31]). The magnetic exchange

parameters were solved by a least-squares mean method. As shown in Fig. 2(b), the in-plane NN exchange interaction J_1 is FM in almost the entire strain range but is converted to AFM when the strain exceeds 6%. It first strengthens and then weakens with the increase of strain, with its maximum strength occurring near the compressive strain of $\sim -2\%$. The in-plane NNN exchange interactions J_2 and J_3 are always AFM and exhibit a nonmonotonic trend with strain. J_2 is slightly larger than J_3, resulting in the wave vector of the spiral and E-type phases always oriented along the b-axis direction. It has been known that the competition between the in-plane NN and NNN exchange interactions, whose magnitude is reflected by the ratio of $|J_2/J_1|$, determines the in-plane spin configuration [44]. The increase of this competition in $R\mathrm{MnO_3}$ bulks causes the transition from the A-type to the spiral and then to the E-type phase [45]. For the strained $\mathrm{LuMnO_3}$ film, as the tensile strain increases, J_1 decays faster than J_2, indicating the increased competition with increasing tensile strain, which can explain the magnetic phase transitions in the region of tensile strain. As the compressive strain further increases, a faster increase in the ratio of $|J_2/J_1|$ leads to a direct transition from FM phase to E_b^*-type phase. The interplane NN exchange interaction J_4 exhibits a nonmonotonic trend similar to that of J_1. It is FM under compressive strain, but is converted to AFM as the tensile strain exceeds $\sim$1%. The interplane NNN exchange interaction J_5 is very weak, so the interplane magnetic coupling is dominated by J_4. Therefore, the transition of the interplane coupling of the magnetic phases from FM to AFM with the increase of strain can be attributed to the change in the sign of J_4.

Previous studies have confirmed that the JT distortion plays an important role in the change of magnetic exchange interactions in $R\mathrm{MnO_3}$ [22,23,46]. The normal Q_3 mode of JT distortion causes the in-plane stagger orbital order of alternating $d_{3x^2-r^2}/d_{3y^2-r^2}$ type similar to that of $R\mathrm{MnO_3}$ bulks. This orbital order leads to a strong FM and a weak AFM e_g-e_g couplings for J_1 and J_4, respectively. The strength and sign of the NN exchange interactions are mainly determined by the competition between the e_g-e_g and the AFM t_{2g}-t_{2g} exchange couplings. The enhancement of Q_3-type JT distortion caused by increasing tensile strain reduces the in-plane NN orbital overlap of the occupied e_g states, leading to a significant weakening of the FM e_g coupling in J_1 [23]. J_4 is less affected since it is dominated by the AFM t_{2g} coupling. As the Q_3-type JT distortion is gradually suppressed by compressive strain, the mixing between the occupied and empty e_g orbitals increases, introducing additional FM exchange within the e_g orbitals. When the Q_3 mode becomes negative with the further increase of compressive strain, the stagger orbital order is transformed into a uniform $d_{3z^2-r^2}$ type (z axis is along the interplane Mn-O_3 bond) [see Fig. 1(a)], introducing AFM e_g coupling for J_1 and J_4. Meanwhile, the FM coupling between the occupied and empty e_g orbitals is gradually reduced due to the increase of splitting by JT distortion. These can explain the changing trend of the NN exchange interactions and the reason why the maximum strength of the NN exchange interactions occurs near the critical strain for the disappearance of Q_3 mode.

In order to reveal the effect of strain on spin orientation, we calculated the magnetic anisotropy energy under various strain. As shown in Fig. 3(a), the b axis is the easy-magnetization axis at zero strain, the same as the $R\mathrm{MnO_3}$ bulks. Figure 3(b) shows that the magnetic anisotropy energy of spins oriented, respectively, along the a and c axes (relative to the b axis) increases monotonously with the increase of strain. However, the c axis turns into the easy-magnetization axis instead of the b axis, as the compressive strain exceeds $\sim -2\%$. This transition is related to the change of orbital order described above. This result indicates that the compressive strain imposed by the square substrates can cause the spin orientation of $\mathrm{LuMnO_3}$ film to change from the in-plane to out-of-plane direction.

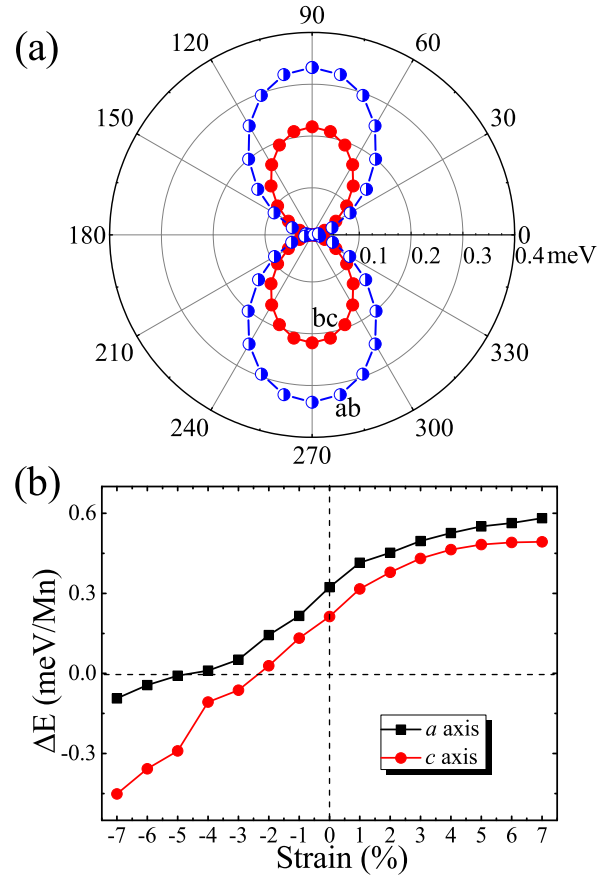

FIG. 3. (a) Dependence of energy on the spin direction under zero strain. The angle denotes the degree of spin direction deviating from the a and c axes, respectively. (b) Change of magnetic anisotropy energy with spins oriented along the a and c axes with strain.

C. Electronic structure

Then we calculated the projected energy bands on the 3d orbitals to reveal the effect of strain on electronic structure. The global cartesian coordinate system was rotated to coincide with the local crystal-field coordinate system. The x, y, z axes are oriented, respectively, along the Mn-O_1, Mn-O_2, and Mn-O_3 bonds in one of the oxygen octahedra. The calculated projected energy bands of up-spin states at strain of 5%, 0, and -5% are shown in Figs. 4(a)–4(c), respectively. For the tensile stain of 5%, the strong Q_3-type JT distortion opens a band gap by splitting the degenerate e_g orbitals. The mixing

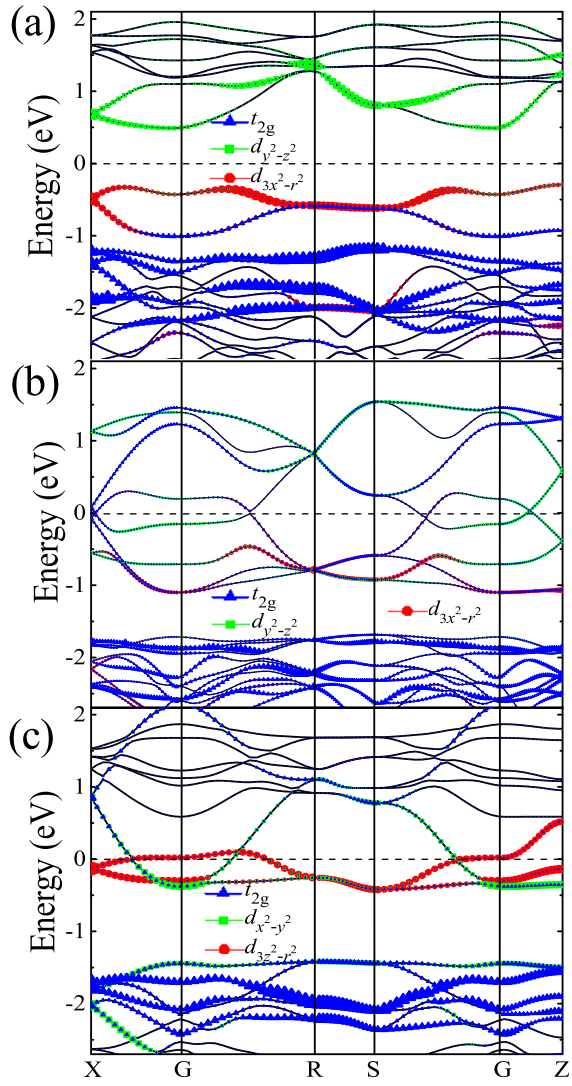

FIG. 4. Projected band structures of up-spin states on the 3*d* orbitals at (a) tensile strain of 5%, (b) 0 strain, and (c) compressive strain of −5%.

between the neighbor e_g orbitals almost disappears shown in the energy band of the occupied $d_{3x^2-r^2}$ state, indicating a weak e_g coupling in the NN exchange interactions. This weakening of e_g coupling caused by the enhancement of JT distortion has been demonstrated in previous studies [23,46]. At zero strain, the occupied and empty e_g orbitals of up-spin states cross near the Fermi level, while a band gap is opened in the down-spin energy bands, confirming a half-metal behavior. The orbital order is significantly weakened due to the reduction of JT distortion. The significant orbital mixing in the occupied e_g states reflects its strong exchange coupling. At compressive strain of −5%, the Fermi level passes through the energy bands of the two e_g states. The increase of gap between the t_{2g} and e_g orbitals shows that the crystal-field splitting is enhanced by compressive strain. The two energy bands of the occupied e_g states near the Fermi level show the same projected orbital of $d_{3z^2-r^2}$ type. The orbital mixing reduces compared with zero strain, indicating the weakening

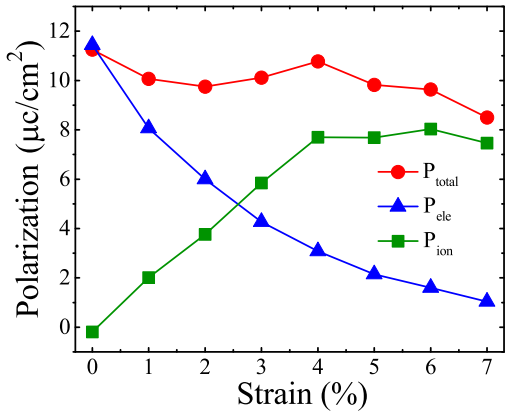

FIG. 5. Total spin-induced polarization P_{total}, pure electronic polarization P_{ele}, and ion-displacement polarization P_{ion} in *E*-type phase changed as a function of strain.

of e_g couplings. These confirm our previous analysis about the causes of change in NN magnetic exchange interactions.

D. Spin-induced ferroelectricity

Similar to the *E*-type multiferroic phase, the E_b^*-type phase present under larger compressive strain can induce polar ion displacements through the exchange-striction mechanism [47]. However, the induced electric polarization will be screened due to its metal behavior. Therefore, we only discuss the spin-induced ferroelectricity in the spiral and *E*-type phases present under tensile strain. Their ferroelectric polarization was calculated using the Berry phase method [48,49]. The atomic positions were optimized by imposing the spiral and *E*-type phases, respectively, to obtain the equilibrium structure of ferroelectric phases, and the optimized structure by imposing the *A*-type phase was treated as the reference paraelectric phase. The calculated ferroelectric polarization of the spiral orders within the range of strain is about $0.09 \sim 0.1\ \mu C/cm^2$, which is about three times the calculated values of spiral order in $TbMnO_3$ and $DyMnO_3$ bulks [23]. The ferroelectric polarization induced by the *E*-type magnetic phase reaches $8.5 \sim 9.8\ \mu C/cm^2$, greater than that of $LuMnO_3$ bulk ($\sim 5.8\ \mu C/cm^2$). This result indicates that the tensile strain imposed by square substrates can improve the spin-induced polarization of the *E*-type multiferroic phase.

We further investigated the impact of the change in structural distortions on the spin-induced polarization of the *E*-type phase. In order to clarify the trend of polarization with strain, the hypothetical *E*-type phase is imposed in the whole range of tensile strain. The contributions of pure electronic (P_{ele}) and ion (P_{ion}) effects to the polarization were distinguished by simultaneously calculating the ferroelectric polarization of the *E*-type phase with the optimized and fixed structures. P_{ion} is included in the former due to the polar displacements being induced by the exchange-striction mechanism, while the latter only contains P_{ele}. As shown in Fig. 5, P_{ele} decreases monotonously with the increasing strain, similar to the trend of J_1. This correlation between P_{ele} and J_1 has been demonstrated in our previous study on strained $RMnO_3$ films [23]. It can be explained as they are both dominated by the in-plane e_g exchange coupling. P_{ion} initially increases linearly with the

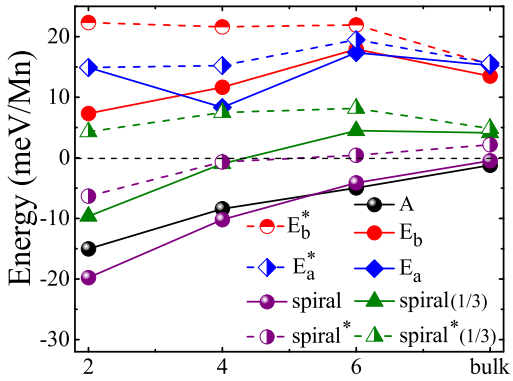

FIG. 6. Dependence of relative energy of the considered AFM orders in the heterostructures on the number of $LuMnO_3$ layers. The results of strain-bulk method are also shown for comparison.

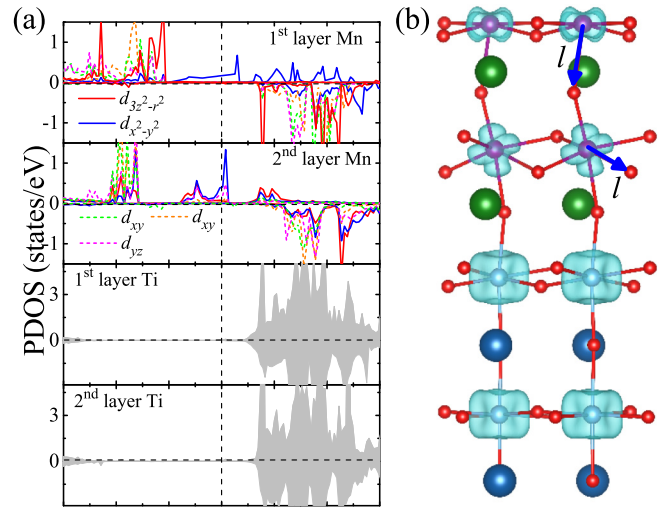

FIG. 7. (a) The layer-resolution projected density of states of d orbitals in the $(LuMnO_3)_2/(SrTiO_3)_2$ heterostructure and (b) the distribution of d holes of the corresponding transition-metal ions shown by deformation charge density. The arrows represent the directions of the polar axis (z axis) of the local crystal field, and the character **l** denotes the longest Mn-O bond.

increasing strain but remains almost unchanged after strain exceeds 4%, just in the vicinity of the phase boundary between spiral and E-type phases. This result indicates that P_{ion} is not always proportional to the strength of JT distortion. It has been known that the P_{ion} mainly arises from the polar displacements of oxygen ions [47], which split the in-plane bond angle into two types. This splitting may be suppressed by the decrease of the in-plane bond angle. Therefore, the trend of P_{ion} with strain is dominated by the competition between the JT distortion and the in-plane rotation distortion of oxygen octahedra. The total polarization varies nonmonotonically with strain due to the opposite trends of P_{ele} and P_{ion}. The latter is dominant at larger strain, so the ferroelectric polarization is mainly derived from the ion-displacement mechanism in the actual E-type phase.

E. $LuMnO_3/SrTiO_3$ heterostructures

We used the $(LuMnO_3)_n/(SrTiO_3)_2$ ($n = 2$, 4, 6) heterostructures to reveal the surface and interface effects in $LuMnO_3$ thin films. The total energy of all considered AFM orders was calculated to determine the magnetic ground state of the heterostructures. The results of strain-bulk model calculated by the same GGA + U ($U_{eff} = 0.5$ eV for Mn) method are also shown for comparison. As shown in Fig. 6, the energy difference between different AFM orders decreases overall with the increasing number of $LuMnO_3$ layers, although all AFM orders do not show a uniform trend. The energy difference of the heterostructure models is significantly larger than that of the strain-bulk model, which can be attributed to the surface reconstruction as discussed below. Interestingly, the surface effect results in a spiral type magnetic ground state when the number of $LuMnO_3$ layers is less than six, while the ground state changes to A-type order with the increasing number of layers, consistent with the strain-bulk model.

The reduction of the coordinate number of Mn ions in the surface layer changes the sign of JT distortion, causing the interplane Mn-O_3 bond to become the longest bond. In order to demonstrate the effect of surface reconstruction on the electronic properties, we calculated the layer-resolution projected density of states of the heterostructures. As shown in Fig. 7(a), for the surface layer of the $(LuMnO_3)_2/(SrTiO_3)_2$ heterostructure, the up-spin $d_{3z^2-r^2}$ orbital is fully occupied, while the up-spin $d_{x^2-y^2}$ orbital is occupied only a small part. The absence of an out-of-plane Mn-O bond significantly reduces the energy of the occupied $d_{3z^2-r^2}$ orbital, making it very close to that of the t_{2g} orbitals. This surface effect caused by the symmetry breaking of the crystal field has been reported in recent study on $LaSrMnO_3$ films grown on $SrTiO_3$ substrate [50]. This $d_{3z^2-r^2}$-type orbital order at the surface is similar to that of the strain-bulk model under large compressive strain. This orbital order is further confirmed by the deformation charge density, which describes the change in electron density before and after bonding. The electron loss region around the Mn ions reflects the distribution of d orbital holes in the crystal field due to the $3d^4$ electron configuration of Mn^{3+} ions. As shown in Fig. 7(b), the Mn ions in the surface layer exhibit the characteristics of $d_{x^2-y^2}$-type hole. The sign of JT distortion and orbital order in the interface layer remain unchanged with respect to the strain-bulk model. However, there is a fairly high density of states near the Fermi level, which is mainly contributed by the $d_{x^2-y^2}$ state. This implies the electron accumulation at the interface, which may be due to charge compensation caused by interfacial polar mismatch. Recently, this interfacial electron accumulation has been confirmed in $LaMnO_3/SrTiO_3(001)$ heterostructure, and the results show that the critical film thickness for the onset of electron accumulation is as thin as two unit cells [51].

For the $(LuMnO_3)_4/(SrTiO_3)_2$ heterostructure, the surface layer has the similar electronic structure and orbital order as the $(LuMnO_3)_2/(SrTiO_3)_2$ heterostructure, as shown in Figs. 8(a) and 8(b). However, for the second layer near the surface, the mode of JT distortion has been changed from the usual two-long and four-short to the four-long and two-short Mn-O bonds, with the shortest bond being the interplane Mn-O_3 bond. This type of JT distortion is common in copper oxides with oxygen octahedral coordination but rare in manganese oxides. The $d_{x^2-y^2}$ orbital is still partially occupied,

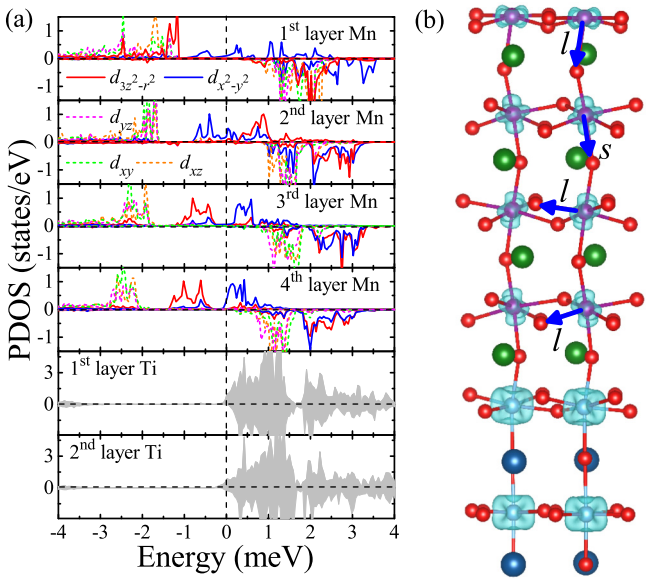

FIG. 8. (a) The layer-resolution projected density of states in the $(LuMnO_3)_4/(SrTiO_3)_2$ heterostructure and (b) the distribution of d holes shown by deformation charge density. The arrows represent the directions of the polar axis (z axis) of the local crystal field. The characters **l** and **s** denote the longest and shortest Mn-O bonds, respectively.

while the $d_{3z^2-r^2}$ orbital is fully unoccupied, resulting in orbital holes dominated by $d_{3z^2-r^2}$ type [see Fig. 8(b)]. For the two layers (third and fourth layers) close to the interface, the mode of JT distortion is normal, similar to that of the $LuMnO_3$ bulk. The splitting between the occupied $d_{3z^2-r^2}$ and unoccupied $d_{x^2-y^2}$ states caused by JT distortion is significant, as shown in Fig. 8(a). At the interface, both the d orbitals of Mn and Ti ions exhibit very small density of states at the Fermi level, which implies that the electron accumulation at the interface decreases dramatically with the increase of the number of layers. The $(LuMnO_3)_6/(SrTiO_3)_2$ heterostructure shows a similar surface effect. The surface reconstruction occurs mainly in the first two layers near the surface of the heterostructures. It changes the sign of JT distortion and results in the reconstruction of orbital order and surface metallization.

IV. CONCLUSIONS

In summary, we have demonstrated the evolution of the magnetic phase and orbital order in $LuMnO_3$ films with strain and revealed the surface and interface effects. The tensile strain enhances the Q_3 mode of JT distortion and causes the emergence of the spiral and E-type multiferroic phases. A FM half-metal phase with high Curie temperature exists in a wide range of compressive strain. A negative Q_3 mode occurs and changes the orbital order when the compressive strain exceeds a certain value, resulting in the emergence of a polar-metal phase. The surface reconstruction occurs mainly in the first two layers near the surface, which is reflected in the change of JT distortion and orbital order. The surface metallization and electron accumulation at the interface have been confirmed in the heterostructure models, while the latter is significantly suppressed with the increase of film thickness.

ACKNOWLEDGMENTS

This work was supported by the National Key Research Program of China (No. 2016YFA0201004), National Natural Science Foundation of China (Grants No. 11974418, No. 11874208, and No. 11804383), the Natural Science Foundation of Jiangsu (Grants No. BK20150173 and No. BK20180637), and the Fundamental Research Funds for the Central Universities (Grant No. 2019QNA30). Computer resources provided by the High Performance Computing Center of China University of Mining and Technology are gratefully acknowledged.

[1] M. B. Salamon and M. Jaime, Rev. Mod. Phys. **73**, 583 (2001).
[2] J. B. Goodenough, Rep. Prog. Phys. **67**, 1915 (2004).
[3] E. Dagotto, Science **309**, 257 (2005).
[4] H.-U. Habermeier, Mater. Today **10**, 34 (2007).
[5] J. M. Rondinelli, S. J. May, and J. W. Freeland, MRS Bull. **37**, 261 (2012).
[6] A. Marthinsen, C. Faber, U. Aschauer, N. A. Spaldin, and S. M. Selbach, MRS Commun. **6**, 182 (2016).
[7] D. G. Schlom, L.-Q. Chen, X. Q. Pan, A. Schmehl, and M. A. Zurbuchen, J. Am. Ceram. Soc. **91**, 2429 (2008).
[8] R. J. Zeches, M. D. Rossell, J. X. Zhang, A. J. Hatt, Q. He, C.-H. Yang, A. Kumar, C. H. Wang, A. Melville, C. Adamo, G. Sheng, Y.-H. Chu, J. F. Ihlefeld, R. Erni, C. Ederer, V. Gopalan, L. Q. Chen, D. G. Schlom, N. A. Spaldin, L. W. Martin *et al.*, Science **326**, 977 (2009).
[9] J. He, A. Borisevich, S. V. Kalinin, S. J. Pennycook, and S. T. Pantelides, Phys. Rev. Lett. **105**, 227203 (2010).
[10] S. J. May, J.-W. Kim, J. M. Rondinelli, E. Karapetrova, N. A. Spaldin, A. Bhattacharya, and P. J. Ryan, Phys. Rev. B **82**, 014110 (2010).
[11] J. H. Haeni, P. Irvin, W. Chang, R. Uecker, P. Reiche, Y. L. Li, S. Choudhury, W. Tian, M. E. Hawley, B. Craigo, A. K. Tagantsev, X. Q. Pan, S. K. Streiffer, L. Q. Chen, S. W. Kirchoefer, J. Levy, and D. G. Schlom, Nature (London) **430**, 758 (2004).
[12] J. H. Lee, L. Fang, E. Vlahos, X. Ke, Y. W. Jung, L. F. Kourkoutis, J.-W. Kim, P. J. Ryan, T. Heeg, M. Roeckerath, V. Goian, M. Bernhagen, R. Uecker, P. C. Hammel, K. M. Rabe, S. Kamba, J. Schubert, J. W. Freeland, D. A. Muller, C. J. Fennie *et al.*, Nature (London) **466**, 954 (2010).
[13] J. H. Lee and K. M. Rabe, Phys. Rev. Lett. **104**, 207204 (2010).
[14] E. Dagotto, T. Hotta, and A. Moreo, Phys. Rep. **344**, 1 (2001).
[15] T. Kimura, T. Goto, H. Shintani, K. Ishizaka, T. Arima, and Y. Tokura, Nature (London) **426**, 55 (2003).
[16] X. Marti, V. Skumryev, C. Ferrater, M. V. García-Cuenca, M. Varela, F. Sánchez, and J. Fontcuberta, Appl. Phys. Lett. **96**, 222505 (2010).
[17] J. S. White, M. Bator, Y. Hu, H. Luetkens, J. Stahn, S. Capelli, S. Das, M. Döbeli, T. Lippert, V. K. Malik, J. Martynczuk, A. Wokaun, M. Kenzelmann, C. Niedermayer, and C. W. Schneider, Phys. Rev. Lett. **111**, 037201 (2013).

[18] Y. W. Windsor, S. W. Huang, Y. Hu, L. Rettig, A. Alberca, K. Shimamoto, V. Scagnoli, T. Lippert, C. W. Schneider, and U. Staub, Phys. Rev. Lett. **113**, 167202 (2014).
[19] X. R. Wang, C. J. Li, W. M. Lü, T. R. Paudel, D. P. Leusink, M. Hoek, N. Poccia, A. Vailionis, T. Venkatesan, J. M. D. Coey, E. Y. Tsymbal, Ariando, and H. Hilgenkamp, Science **349**, 716 (2015).
[20] Y. F. Kou, T. Miao, H. Wang, L. Xie, Y. M. Wang, H. X. Lin, S. S. Wang, H. Liu, Y. Bai, Y. Y. Zhu, J. Shao, P. Cai, W. B. Wang, H. F. Du, X. Q. Pan, R. Q. Wu, L. F. Yin, and J. Shen, J. Mater. Chem. C **5**, 7813 (2017).
[21] K. Shimamoto, S. Mukherjee, N. S. Bingham, A. K. Suszka, T. Lippert, C. Niedermayer, and C. W. Schneider, Phys. Rev. B **95**, 184105 (2017).
[22] J. T. Zhang, C. Ji, Y. Y. Shangguan, B. X. Guo, J. L. Wang, F. Z. Huang, X. M. Lu, and J. S. Zhu, Phys. Rev. B **98**, 195133 (2018).
[23] J. T. Zhang, C. Ji, J. L. Wang, W. S. Xia, X. M. Lu, and J. S. Zhu, Phys. Rev. B **97**, 085124 (2018).
[24] C. W. Schneider, S. Mukherjee, K. Shimamoto, S. Das, H. Luetkens, J. S. White, M. Bator, Y. Hu, J. Stahn, T. Prokscha, A. Suter, Z. Salman, M. Kenzelmann, T. Lippert, and C. Niedermayer, Phys. Rev. B **94**, 054423 (2016).
[25] G. N. Li, X. K. Huang, J. S. Hu, G. Song, and W. Y. Zhang, Phys. Rev. B **97**, 085140 (2018).
[26] E. Breckenfeld, A. B. Shah, and L. W. Martin, J. Mater. Chem. C **1**, 8052 (2013).
[27] J. Fontcuberta, C. R. Phys. **16**, 204 (2015).
[28] S. Venkatesan, C. Daumont, B. J. Kooi, B. Noheda, and J. T. M. De. Hosson, Phys. Rev. B **80**, 214111 (2009).
[29] P. E. Blöchl, Phys. Rev. B **50**, 17953 (1994).
[30] G. Kresse and J. Furthmüller, Phys. Rev. B **54**, 11169 (1996).
[31] See Supplemental Material at http://link.aps.org/supplemental/10.1103/PhysRevB.100.174417, which includes Ref. [32], for (1) change of magnetic ground state of $LuMnO_3$ bulk with U value, (2) comparison of projected band structures calculated by PBE and HSE functionals, (3) testing the effect of the number of $SrTiO_3$ layers in the heterostructure models, and (4) computational details of magnetic exchange interactions.
[32] A. Stroppa and S. Picozzi, Phys. Chem. Chem. Phys. **12**, 5405 (2010).
[33] R. I. Eglitis, Appl. Surf. Sci. **358**, 556 (2015).
[34] R. I. Eglitis and A. I. Popov, J. Saudi Chem. Soc. **22**, 459 (2018).
[35] Y. F. Hsiao, J. Y. Lai, J. Y. Lin, H. W. Fang, Y. T. Hung, C. W. Luo, K. H. Wu, T. M. Uen, J. Y. Lin, and J. Y. Juang, Appl. Phys. Express **6**, 103201 (2013).
[36] M. An, Y. K. Weng, H. M. Zhang, J.-J. Zhang, Y. Zhang, and S. Dong, Phys. Rev. B **96**, 235112 (2017).
[37] D. D. Cuong, B. Lee, K. M. Choi, H.-S. Ahn, S. Han, and J. Lee, Phys. Rev. Lett. **98**, 115503 (2007).
[38] H. Sawada, Y. Morikawa, K. Terakura, and N. Hamada, Phys. Rev. B **56**, 12154 (1997).
[39] Y. S. Hou, J. H. Yang, X. G. Gong, and H. J. Xiang, Phys. Rev. B **88**, 060406(R) (2013).
[40] R. Qiu, E. Bousquet, and A. Cano, J. Phys.: Condens. Matter **29**, 305801 (2017).
[41] D. Rubi, C. de Graaf, C. J. M. Daumont, D. Mannix, R. Broer, and B. Noheda, Phys. Rev. B **79**, 014416 (2009).
[42] X. Marti, V. Skumryev, A. Cattoni, R. Bertacco, V. Laukhin, C. Ferrater, M. V. García-Cuenca, M. Varela, F. Sánchez, and J. Fontcuberta, J. Magn. Magn. Mater. **321**, 1719 (2009).
[43] F. Jiménez-Villacorta, J. A. Gallastegui, I. Fina, X. Marti, and J. Fontcuberta, Phys. Rev. B **86**, 024420 (2012).
[44] K. Yamauchi, F. Freimuth, S. Blügel, and S. Picozzi, Phys. Rev. B **78**, 014403 (2008).
[45] T. Kimura, S. Ishihara, H. Shintani, T. Arima, K. T. Takahashi, K. Ishizaka, and Y. Tokura, Phys. Rev. B **68**, 060403(R) (2003).
[46] I. Solovyev, N. Hamada, and K. Terakura, Phys. Rev. Lett. **76**, 4825 (1996).
[47] I. A. Sergienko, C. Sen, and E. Dagotto, Phys. Rev. Lett. **97**, 227204 (2006).
[48] R. D. King-Smith and D. Vanderbilt, Phys. Rev. B **47**, 1651 (1993).
[49] D. Vanderbilt and R. D. King-Smith, Phys. Rev. B **48**, 4442 (1993).
[50] Y. Li, E. Choi, S.-I. Kim, S.-H. Baek, S.-Y. Park, Y. Jo, and J. Seo, AIP Advances **7**, 085224 (2017).
[51] Z. H. Chen, Z. H. Chen, Z. Q. Liu, M. E. Holtz, C. J. Li, X. R. Wang, W. M. Lü, M. Motapothula, L. S. Fan, J. A. Turcaud, L. R. Dedon, C. Frederick, R. J. Xu, R. Gao, A. T. N'Diaye, E. Arenholz, J. A. Mundy, T. Venkatesan, D. A. Muller, L.-W. Wang *et al.*, Phys. Rev. Lett. **119**, 156801 (2017).